Chapter 6
Improvement in white light emission of Dy^{3+} doped $CaMoO_4$ via Zn^{2+} co-doping

"Chapter 6 presents the enhancement of the photoluminescence properties of Dy^{3+} doped $CaMoO_4$ phosphors with co-doping of Zn^{2+} ion. The chapter presents the structural and elemental properties investigated by XRD, SEM, TEM, FTIR, and XPS. The Zn^{2+} co-doping improves the crystallinity of the $CaMoO_4$:4%Dy^{3+} phosphor by reducing the defect levels which is explained in detail in the XPS section. The chapter shows the correlation between the change in crystallinity and the improvement in luminescence by Zn^{2+} co-doping. Moreover, the thermal stability of 0.25% Zn^{2+} co-doped $CaMoO_4$:4%Dy^{3+} phosphor has also been investigated. Therefore, this chapter opens new avenues for development as excellent single-component white light emitters for various optoelectronic applications."

6.1 Introduction

For the past two decades, White Light Emitting Diodes (wLEDs) have been increasingly preferred over traditional light sources due to their unique properties such as environmental friendliness, longer operating lifetime, electric energy saving, enhanced optical power, and higher luminous efficacy.[115,169] Nowadays commercial wLEDs are prepared by depositing Ce^{3+} doped $(Y,Ga)_3(Al,Ga)_5O_{12}$ yellow phosphor onto InGaN blue chips to emit white light.[66,67] White light emission can also be realized by the combination of red, blue, and green multiphase phosphors. However, several drawbacks in this technique due to multistage phosphors, such as adjustment of color ratio, color re-absorption, emission efficiency, etc.[172,173] Therefore, the solution to these shortcomings is a single component phosphor that gives excellent white light emission with near Ultraviolet (UV) absorption.

Various phosphors have been studied as the host for white-light-emitting phosphors. Many of these previously published host phosphors have several drawbacks such as Ca_2SiO_4, CaF_2, which are prepared by complex synthesis processes whereas, hosts such as $SrWO_4$, $CaSrAl_2SiO_7$ have limited thermal and chemical stability, making them difficult to produce on a large scale[188,120,121,174]. Therefore, importance has been given to the quest to develop thermally and chemically stable phosphors that can be prepared via environment-friendly and cost-effective technology. Molybdates such as $CaMoO_4$ have gained special attention in the research fraternity due to their potentiating properties. The $CaMoO_4$ shows a tetragonal crystal structure with self-activated broadband emission lying in the visible light region. The advantages of $CaMoO_4$ host phosphor over other phosphors are that $CaMoO_4$ possesses good chemical and thermal stability, a longer average decay lifetime (14 ms), and a higher melting point (1435-1480 °C).[89] The $CaMoO_4$ phosphor can be prepared through various synthesis processes such as auto-combustion, solid-state technique, sol-

gel, solvothermal/hydrothermal, and one-step spray pyrolysis, etc[22,7577,78,124], among which the auto-combustion process (urea fuel-based) is advantageous over others because of its ease and cost-effectiveness. These properties of $CaMoO_4$ make it a better host material.

The various rare-earth (Re^{3+}) doped $CaMoO_4$ phosphors have become increasingly important owing to their remarkable optical properties. These materials are being widely investigated in the fields of optoelectronics and medical devices such as display devices[66], white-light-emitting diodes (w-LEDs)[24], optical fiber[175], semiconductor laser[177], photo-catalysis[12], temperature sensors[105], bio-imaging[74], etc. The Re^{3+} doped $CaMoO_4$ phosphors are significantly better than other traditional phosphors due to their sharp spectral emissions covering UV to Near Infrared (IR) region and also depict color tunability due to the different arrangements of the 4f electrons. Among all Re^{3+} ions, the Dy^{3+} ion is studied with various spectroscopy techniques because its spectroscopic properties are very sensitive to its local environment in the host matrix. The Dy^{3+} ion is used as a dopant in various host materials for different applications, some of which are listed in Table 1.

Table 6.1 Various applications of Dy^{3+} doped phosphors.

S. No.	Application	Material	Ref.
1.	White-light emitting phosphors	Dy^{3+} doped $NaSr_2Nb_5O_{15}$, Dy^{3+} doped $Ba_5CaAl_4O_{12}$, Dy^{3+} doped Sr_2SiO_4, Dy^{3+} doped $LiSr_4(BO_3)_3$, Dy^{3+} doped Li_2SrSiO_4,	25 26 8 11 199
2.	Laser application	Dy^{3+} doped ZBLAN laser, Dy^{3+}doped Aluminosilicate fiber	200 201
3.	Photo-catalytic application	Dy^{3+} doped $SrMoO_4$,	190
4.	Temperature sensing	Dy^{3+} doped $Y_4Al_2O_9$,	32

		Dy^{3+} doped Al_2O_3,	202
5.	UV Sensor application	Dy^{3+} doped ZnO-Al_2O_3-B_2O_3, Dy^{3+} doped ZnO,	31 203
6.	Bio-sensing	Eu^{2+},Dy^{3+} doped $(Sr_{1-\delta}Ba_\delta)_2MgSi_2O_7$,	204
7.	Latent fingerprint detection	Eu^{2+}/ Dy^{3+} doped $SrAl_2O_4$,	29

The Dy^{3+} ions present two predominant luminescence bands lying in the blue and yellow spectral regions corresponding to the $^4F_{9/2} \rightarrow {}^6H_{15/2}$ and $^4F_{9/2} \rightarrow {}^6H_{13/2}$ electronic transitions, respectively [26]. White light emission may be easily obtained due to the adjustment of the ratio of blue and yellow spectral bands of the Dy^{3+} ions. Thus, Dy^{3+} doped luminescent material emits white light in the form of a single-ingredient phosphor, addressing the shortfalls of commercial wLEDs. As a result, the possibility of obtaining white light with high luminous efficiency increases. There are some reports on Dy^{3+} doped materials such as $NaSr_2Nb_5O_{15}$[25], $Ba_5CaAl_4O_{12}$[26], $LiSr_4(BO_3)_3$[11], and $Ca_2MgSi_2O_7$[36] for white light emission, but these phosphors have several shortcomings such as weak self-activated emission and synthesized via high-temperature solid-state processes. However, there are no such drawbacks in the Dy^{3+} doped $CaMoO_4$ phosphor.

In this chapter, the increase in the emission intensity of Dy^{3+} doped $CaMoO_4$ phosphor via Zn^{2+} co-doping is reported. The phosphors were synthesized via a lucrative auto-combustion method. The PL spectra of all samples were studied and observed that the PL emission intensity of the Dy^{3+} transitions enhances up to 34 percent by 0.25% co-doping of Zn^{2+} ion. The CIE coordinates (x, y) for the 0.25% Zn^{2+} co-doped phosphor are (0.319, 0.381), which is very close to proper white emission, and the color purity is very low around ~10%. Our results show that improved white emission may be obtained by optimum Zn^{2+}

co-doping. Thus, Zn^{2+}/Dy^{3+} doped $CaMoO_4$ as a single-ingredient phosphor might be a potential candidate for white light-emitting diodes (wLEDs).

All the phosphors developed in this chapter are prepared by the urea-assisted internal combustion process, which has been described in detail in Chapter 2, in addition, all the characterization techniques and their models used in this chapter have been described in Chapter 2.

6.2 Results and discussion

6.2.1 XRD analysis

The X-ray diffraction patterns of CMO, Dy4, and Z0.25 samples are shown in Fig. 6.1(a—c). Some intense diffraction peaks are indexed in the XRD pattern which matches well with the crystallographic card JCPDS file # 85–1267 (a=b=5.223 Å, c=11.429 Å).[45] All phosphors show a highly crystalline tetragonal structure with space group symmetric $I4_1/a$. The tetragonal structure of $CaMoO_4$ constitutes $[CaO_8]$ dodecahedral clouds and $[MoO_4]$ tetrahedral clouds which are connected by Ca–O–Mo edges as shown for the Z0.25 sample in Fig. 6.1(d). The lattice parameters and unit cell volume of all prepared samples have been calculated by refinement of XRD patterns via FULLPROF software[85]. Fig. 6.2(a) shows the variation of unit cell volume and lattice parameters (in inset) of all prepared phosphors. The lattice parameters and unit cell volume are a=5.2278 Å, c=11.4404 Å, and V=312.6649 $Å^3$ for CMO phosphor as tabulated in Table 6.2. The lattice parameters and unit cell volume are decreased with Dy^{3+} doping in $CaMoO_4$ phosphor. After Zn^{2+} co-doping in $CaMoO_4$: 4%Dy^{3+} phosphor, the lattice parameters, and unit cell volume further decrease, because the ionic radii of Dy^{3+} ion (1.02 Å) and Zn^{2+} ion (0.9 Å) are lesser than Ca^{2+} ionic radii (1.12 Å)[87], which ensures that Dy^{3+} and Zn^{2+} ions have occupied sites of

Ca^{2+} ions. The unit cell volume and lattice parameters of CMO, Dy4, and Z0.25 phosphor are tabulated in Table 6.2. The average crystallite size of all prepared phosphors has been calculated via Williamson-Hall (W–H) method with the given expression [138,148];

$$\beta_{calc}cos\theta = 4\epsilon sin\theta + \frac{K\lambda}{D} \quad 6.1$$

Where β_{calc} is Full width at half maxima (FWHM) of XRD peak corresponds to peak position 2θ, which is calculated by subtracting instrument peak FWHM (β_{inst}). λ is the X-rays wavelength (1.54 Å) used in XRD analysis. K is a shape factor (~0.9). D and ϵ represent the average crystallite size, and lattice strain of the phosphors, respectively. The $\beta_{calc}cos\theta$ versus $sin\theta$ plot in the Williamson-Hall formula shows a linear equation. The intercept of the linearly fitted curve gives information on average crystallite size (D) and the slope gives information about lattice strain (ϵ). The calculated average crystallite size of the CMO sample is 67 nm. The crystallite size increases with increasing the concentration of Dy^{3+} ions, which indicates the crystalline nature of phosphor enhanced with Dy^{3+} doping. The average crystallite size of Dy4 phosphor is 70 nm. The average crystallite size increases with increasing the Zn^{2+} co-doping concentration up to Z0.25 and thereafter reduces on further increasing the co-doping concentration. The probability of substitution of Zn^{2+} ions at the interstitial lattice sites increases with increasing the concentration of Zn^{2+}. Thereby, the distortion in the lattice increases. Hence, the crystallite size decreases for Z0.5 and Z1 phosphors. Fig. 6.2(b) depicts the variation of the crystallite size for different phosphors and the corresponding values are tabulated in Table 6.2.

The calculated lattice strain of prepared phosphors represents the existence of lattice distortions due to the crystal defects. The calculated lattice strain of prepared phosphors is depicted in the inset of Fig. 6.2(b) and listed in Table 6.2. The calculated lattice strain of

the CMO sample is 0.0016 and the lattice strain of Dy^{3+} doped phosphor decreases with increasing the doping concentration. After Zn^{2+} co-doping in the Dy4 sample, the lattice strain remains almost the same with increasing the co-doping concentration. The approximate value of the lattice strain of Dy4 and Z0.25 samples are 0.0004. The improved crystalline nature and decreased lattice strains imply that defects in the crystal are decreased which helps to improve the luminescence intensity[205].

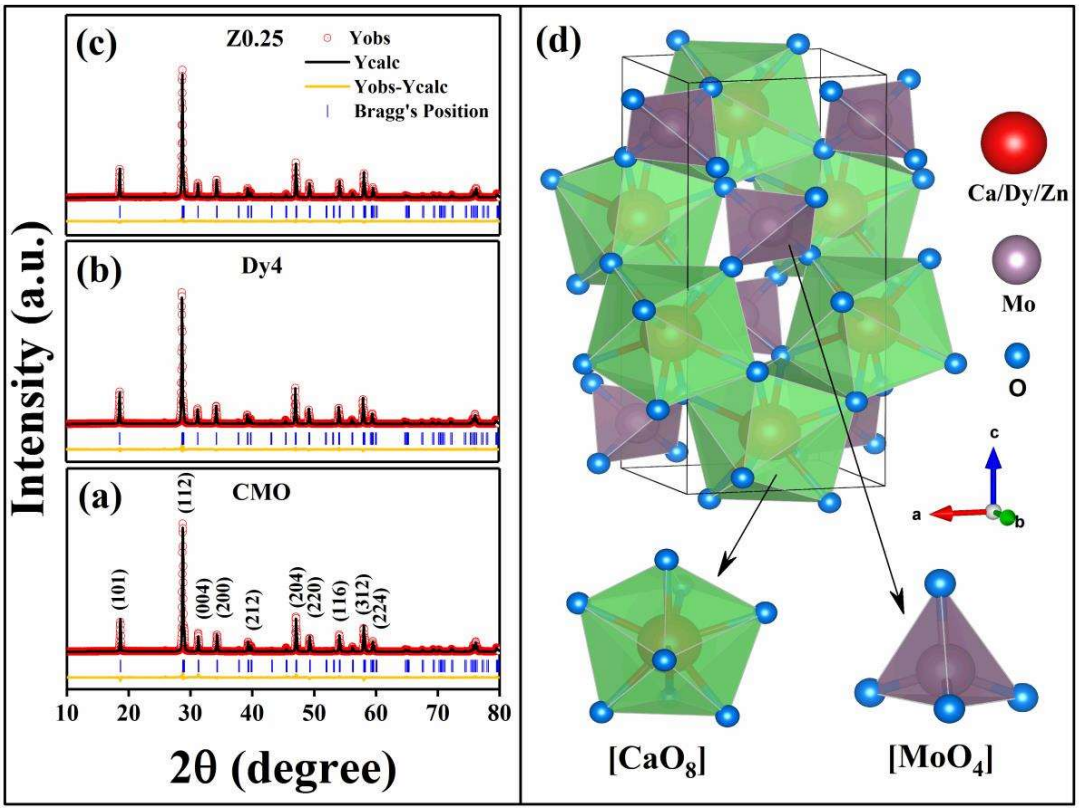

Fig. 6.1 Rietveld refined XRD patterns for **(a)** CMO, **(b)** Dy4, **(c)** Z0.25 samples, and **(d)** crystal structure of the Z0.25 sample.

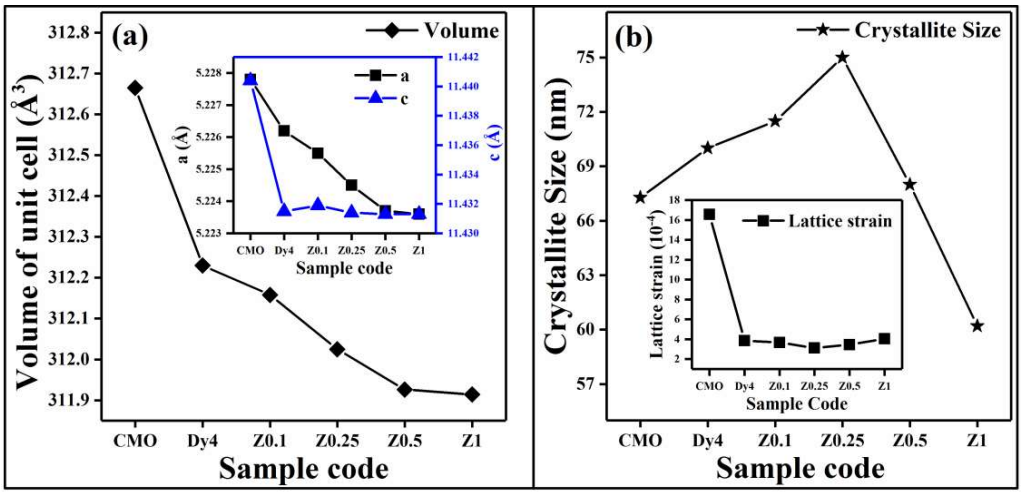

Fig. 6.2 (a) Variation of unit cell volume and lattice parameters (Inset) with Zn^{2+} co-doping and **(b)** Variation of Crystallite size and lattice strain (Inset) with Zn^{2+} co-doping.

Table 6.2 Structural parameters obtained from Rietveld refinement XRD patterns.

Parameters	CMO	Dy4	Z0.25
Lattice parameter (a, c) (Å)	a=5.2278, c=11.4404	a=5.2262, c=11.4315	a=5.2255, c=11.4314
Angles (α, β, γ)	(90, 90, 90)	(90, 90, 90)	(90, 90, 90)
Wyckoff positions Ca (x, y, z) Mo (x, y, z) O (x, y, z)	Ca (0, 0.25, 0.625) Mo (0, 0.25, 0.125) O (0.1561, -0.0137, 0.206)	Ca (0, 0.25, 0.625) Mo (0, 0.25, 0.125) O (0.1496, 0.0023, 0.2075)	Ca (0, 0.25, 0.625) Mo (0, 0.25, 0.125) O (0.1508, -0.0069, 0.2092)
The volume of unit cell (Å³)	312.6649	312.2304	312.1441
Mo—O	1.784	1.830	1.848
Ca—O1	2.445	2.414	2.378
Ca—O2	2.457	2.423	2.434
χ^2	6.18	4.32	5.04
Crystallite size (nm)	67	70	75
Lattice strain (10^{-4})	16.55	3.85	3.12

6.2.2 SEM Images analysis

SEM images of CMO, Dy4 and Z0.25 phosphors are shown in Fig. 6.3. These images demonstrate aggregated spherical particle shape of all phosphors. The particle agglomeration is caused by the formation of covalent or/and metallic bonds, affected by dopants. The average particle size has been calculated by using ImageJ software. For CMO phosphor, the average particle size is 0.8 μm. The calculated particle size of Dy4 and Z0.25 is 1.13 μm and 1.36 μm, respectively. The average particle size is improved by Zn^{2+} co-doping. A particle is formed by a combination of crystallites. Therefore, the size of the particle is in order of μm. The increasing particle size of the phosphor indicates an increase in its crystallite size.

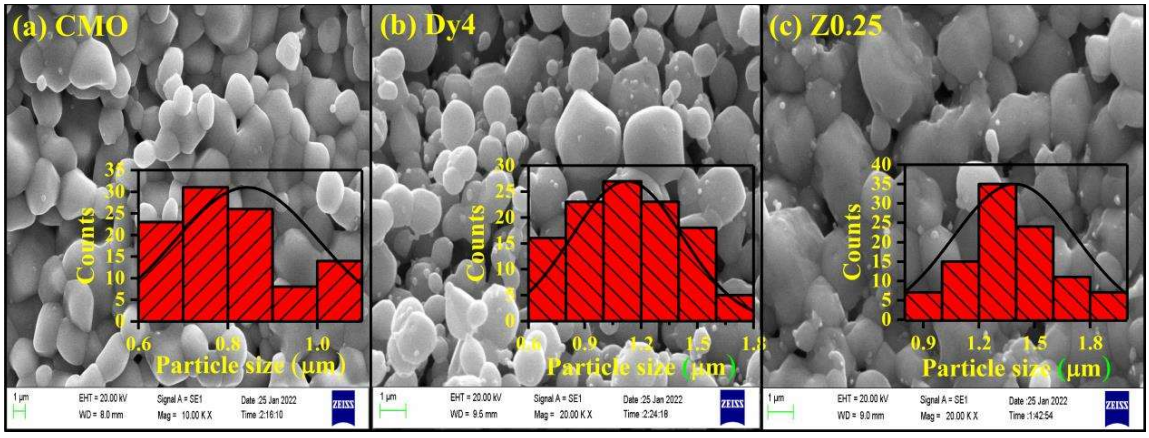

Fig. 6.3 SEM images of **(a)** CMO and **(b)** Dy4 and (c) Z0.25 samples.

6.2.3 EDX analysis

Energy dispersive X-ray (EDX) has been performed to investigate the elemental composition of all the samples. EDX spectra in Fig. 6.4 confirm all elements present in CMO, Dy4, and Z0.25 and verify that the sample does not contain any foreign element

impurities. The atomic and weight percentages of the elements obtained from the EDX analysis and their required amount used in the synthesis process are tabulated in Table 6.3.

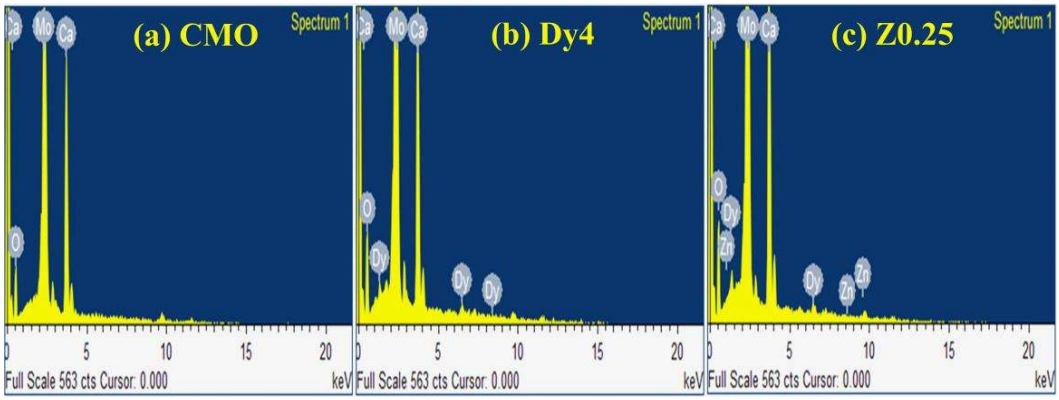

Fig. 6.4 EDX spectra for **(a)** CMO, **(b)** Dy4 and (c) Z0.25 samples.

Table 6.3 Comparison of EDX results with stoichiometric amount.

Sample		**EDX results**		**Stoichiometric amount**	
		Weight %	**Atomic %**	**Weight %**	**Atomic %**
CMO	**Ca**	22.23	19.47	22.03	16.67
	Mo	49.28	18.03	47.97	16.67
	O	28.49	62.50	32	66.67
Dy4	**Ca**	19.10	16.91	18.78	16.00
	Mo	47.85	17.70	46.82	16.67
	O	29.09	64.52	31.23	66.67
	Dy	3.96	0.87	3.17	0.67
Z0.25	**Ca**	19.32	16.68	18.72	15.95
	Mo	47.16	17.16	46.80	16.67
	O	30.47	65.45	31.22	66.67
	Dy	2.94	0.64	3.17	0.67
	Zn	0.11	0.06	0.08	0.04

6.2.4 TEM images analysis

The morphology of the phosphor has been studied by transmission electron microscopy (TEM). In Fig. 6.5(a, b), the TEM images of the Dy4 and Z0.25 phosphors depict the aggregated spherical-shaped particles. The range of nanoparticle size is 10 nm to 60 nm for both phosphors. Fig. 6.5(c) shows the rings of selected area electron diffraction (SAED) patterns which correspond to (101), (112), (004), (200), (204), (212), and (116) planes of the tetragonal crystal structure of Z0.25 phosphor[157]. Fig. 6.5(d) shows the high-resolution TEM image for the Z0.25 phosphor in which clear lattice fringes are observed. The lattice spacing of the fringes is obtained by fast Fourier transform (FFT) using ImageJ software. The obtained lattice spacing of the 004 planes is 0.286 nm[157].

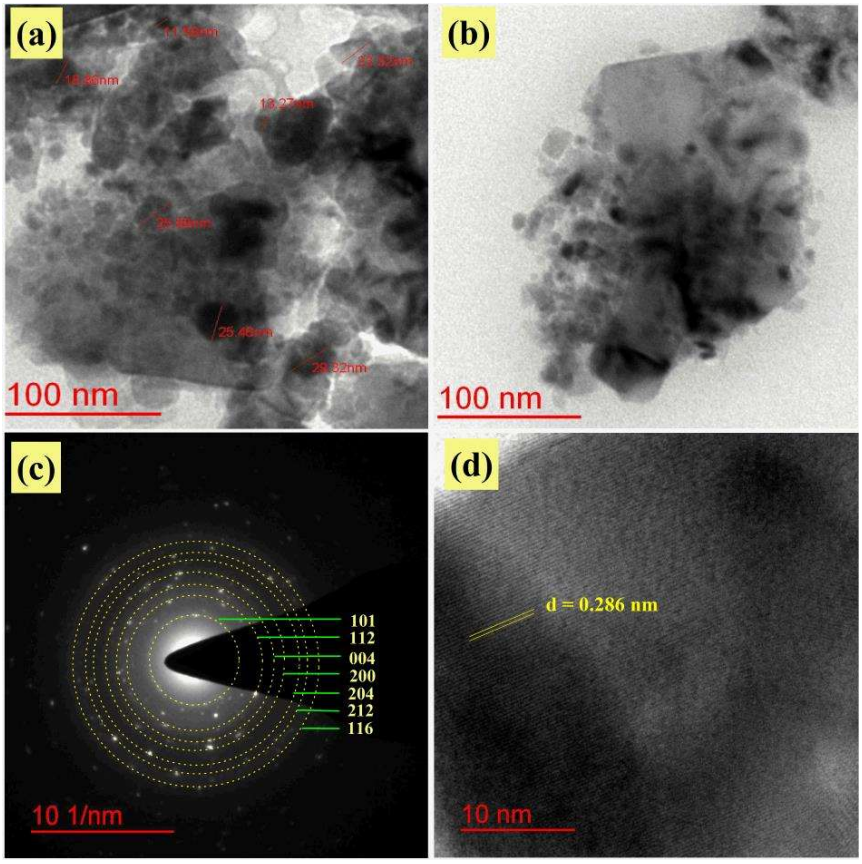

Fig. 6.5 TEM images of **(a)** Dy4, **(b)** Z0.25 samples, **(c)** SAED pattern for Z0.25 sample and **(d)** High-resolution TEM of Z0.25 sample.

6.2.5 XPS analysis

The chemical states of all the elements present in CMO, Dy4, and Z0.25 samples have been investigated via X-ray photoelectron spectroscopy (XPS). XPS survey scans of CMO, Dy4, and Z0.25 samples are shown in Fig. 6.6(f), consisting of significant peaks of Ca, Mo, O, Dy, and Zn, indexed in the figure. The XPS spectra of all the elements are depicted in Fig. 6.6(a—e). In Fig. 6.6(a), two major peaks located near 350.48 eV and 346.98 eV, correspond to bound states $2p_{1/2}$ and $2p_{3/2}$ of Ca^{2+} ion, respectively. These binding energy peaks manifest +2 oxidation state of calcium in all samples. Two peaks observed near 235.58 eV and 232.38 eV in XPS spectra of Mo3d (Fig. 6.6(b)) are related to bound states $3d_{3/2}$ and $3d_{5/2}$ of molybdenum ions, which confirms that molybdenum ions are present in

their Mo^{6+} state in all phosphors. Fig. 6.6(c) shows the XPS spectra of O1s level, fitted with Gaussian curve with a combination of two symmetric peaks O_L and O_V centered near 530.38 eV and 531.68 eV, respectively. O_L peak is attributed to surface lattice oxygen, and O_V peak is assigned to surface oxygen vacancies. These binding energy peaks of the O1s core level manifest a -2 chemical state of oxygen in all phosphors. The bound energy positions of Ca2p, Mo3d, and O1s core levels are well-matched with earlier reported values for $CaMoO_4$ phosphor.[89,185] The larger surface-to-volume ratio in nanoparticles creates a lot of surface bonds associated with oxygen vacancies. These oxygen vacancies are created defect levels below the conduction band in the forbidden energy region and the trapped electrons in these defect states produce non-radiative emissions[91]. Oxygen vacancy concentration has been evaluated by comparing the relative area ratio of the O_V and O_L peaks, the area ratio of the O_V and O_L peaks for CMO is 0.59, which reduces to 0.56 for Dy4 and further decreases up to 0.21 for the Z0.25 phosphor, which confirms that Z0.25 phosphor has the least concentration of oxygen vacancy among all the samples and correspondingly, Z0.25 phosphor has the least amount of defect levels associated with oxygen vacancy. It can also be verified from the increased crystallite size of the doped and co-doped phosphors in the XRD section. The increased crystallite size reflects a decrease in the surface-to-volume ratio which reduces the defect levels of surface-associated oxygen vacancies and leads to an enhancement in the overall PL emission by reducing the probability of non-radiations transitions.

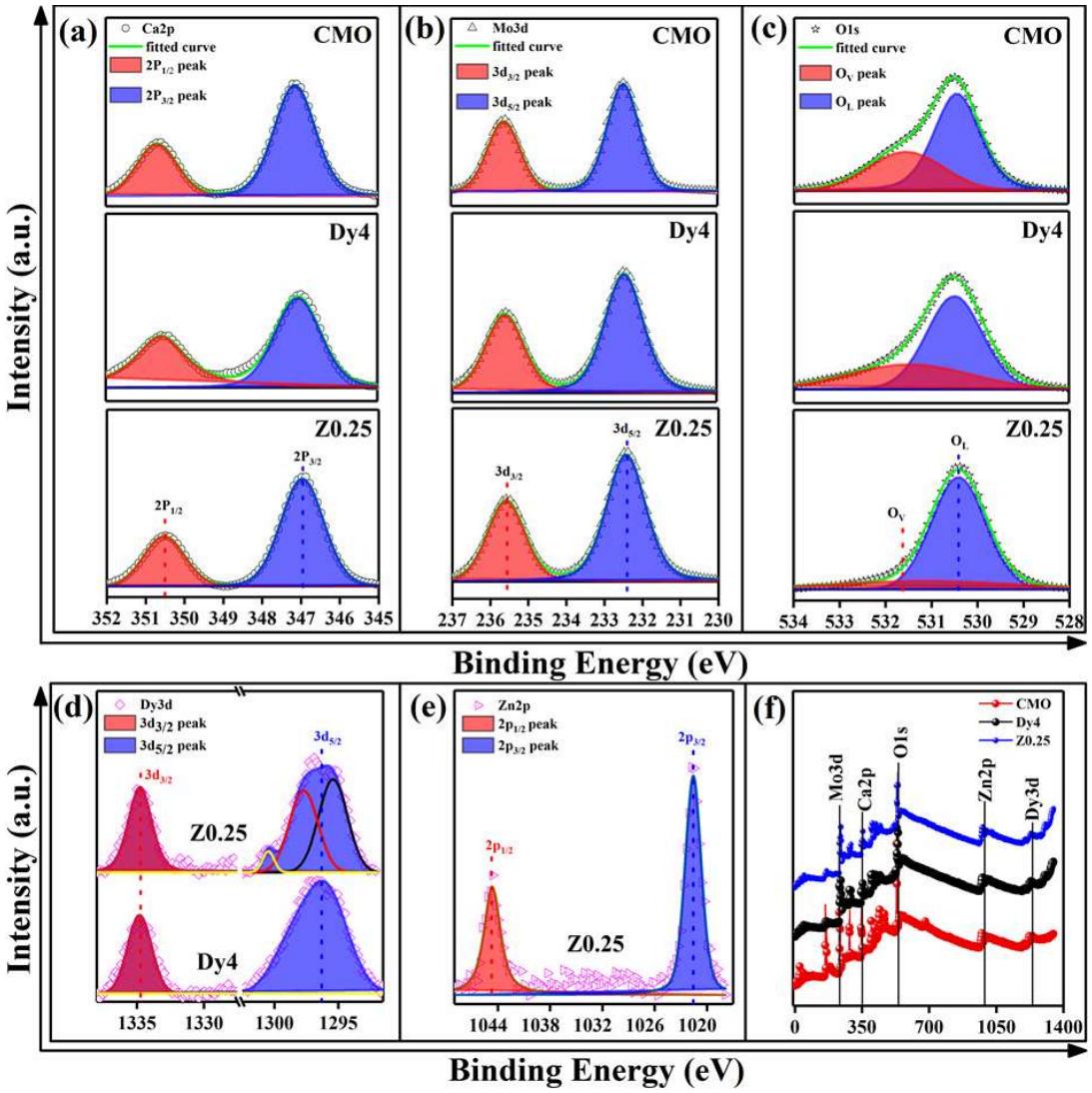

Fig. 6.6 XPS scan of **(a)** Ca2p, **(b)** Mo3d, and **(c)** O1s for CMO, Dy4 and Z0.25 samples, XPS scan of **(d)** Dy3d, **(e)** Zn2p for Dy4 and Z0.25, and **(f)** XPS survey for CMO, Dy4, and Z0.25 samples.

Fig. 6.6(d) demonstrates XPS scan of Dy3d core levels for Dy4 and Z0.25 phosphor. The two bands centered at 1334.88 eV and 1296.28 eV are attributed to the bound states $3d_{3/2}$ and $3d_{5/2}$ of Dy3d core. The lower binding energy band (~1296.28 eV) shows an asymmetric nature arising due to spin-orbit splitting in Dy3d level and therefore it can be deconvoluted into two or more symmetric peaks[18]. For the Z0.25 sample, this band is deconvoluted into three symmetric peaks centered at 1295.28 eV, 1297.88 eV, and 1300.4

eV, respectively. The binding energy bands of Dy3d core level confirm that dysprosium ions are present in +3 chemical states[18,185]. In Fig. 6.6(e), two bands centered at ~1044.68 eV and ~1021.68 eV are observed in Zn2p XPS spectra for the Z0.25 phosphor, which is related to $2p_{1/2}$ and $2p_{3/2}$ bound states of Zn2p, respectively, and manifest +2 chemical state of zinc ions[206].

6.2.6 FTIR analysis

The FTIR spectra (Fig. 6.7(a)) are used to study the vibrational modes present in CMO, Dy4, and Z0.25 samples. There are 26 different vibrational modes present in $CaMoO_4$ type crystals, represented by the following expression [96]:

$$\Gamma = \left(3A_g + 5B_g + 5E_g\right) + \left(5A_u + 3B_u + 5E_u\right) \quad 6.2$$

Out of the 26 vibrational modes, 13 modes $(3A_g + 5B_g + 5E_g)$ are Raman active, and 8modes $(4A_u + 4E_u)$ are IR active vibrational modes. Two prominent vibrational bands of the $[MoO_4]^{2-}$ are observed in the 400 cm^{-1} to 1400 cm^{-1} fingerprint region. One of them is centered at ~769.45 cm^{-1} and is due to the anti-symmetric stretching vibration of the O–Mo–O bond. The second band centered at ~429.8 cm^{-1} is due to the bending of Mo–O bonds which correspond to the A_u and E_u modes. These vibrational bands validate that $[MoO_4]^{2-}$ clouds of $CaMoO_4$ phosphor. Some additional bands are observed in the FTIR spectra due to deformations of the C—C/C—N ring, C—H & O—H bonds, and stretching vibration of CO & CO_2 molecules. The information on all the vibrational bands present in the three phosphors is tabulated in Table 6.4.

Table 6.4 Vibrational modes of CMO, Dy4, and Z0.25 samples.

CMO	Dy4	Z0.25	Vibrational mode	Ref.
426	426	426	Mo—O bending	[18]
771	771	771	O—Mo—O stretching	[18]
1215, 1369	1216, 1370	1216, 1370	C—C, C—N, C—H, O—H band	[207]
1743	1743	1743	C=O stretching	[207]
2358	2358	2358	O=C=O stretching	[207]

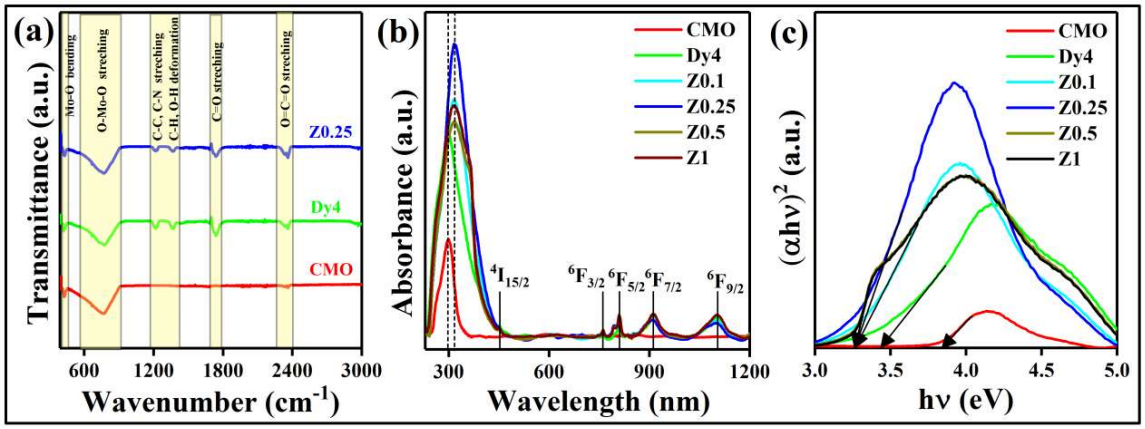

Fig. 6.7 (a) FTIR spectra for CMO, Dy4, and Z0.25 samples, **(b)** UV-Vis absorption spectra, and **(c)** Tauc plot for CMO, Dy4, Z0.1, Z0.25, Z0.5, and Z1 samples.

6.2.7 Absorption analysis

Fig. 6.7(b) shows the absorption spectra of the prepared phosphors in the range of wavelength from 200 nm to 1200 nm. A broad absorption band centered near 300 nm is observed for the CMO sample, attributed to the charge transfer band from O^{2-} to Mo^{6+} bands. The absorption band width increases with Dy^{3+} doping due to the overlap of two bands corresponding to charge transfer O^{2-} to Mo^{6+} and O^{2-} to Dy^{3+}.[18] Some absorption peaks of Dy^{3+} ion are observed near 453 nm, 762 nm, 813 nm, 910 nm, and 1105 nm, ascribed to the electronic transitions from $^6H_{15/2}$ ground level to $^4I_{15/2}$, $^6F_{3/2}$, $^6F_{5/2}$, $^6F_{7/2}$, and $^6F_{9/2}$ excited levels of Dy^{3+} ion, respectively. The absorption peak positions are in good agreement with earlier reported results by Suthanthira kumar *et al.* [191]. A red-shift from

~300 nm to ~314 nm is observed in the peak position of the absorption band for Zn^{2+} co-doped samples (Fig. 6.7(b)), owing to the reduction in the optical bandgap. The absorption band width further increases with Zn^{2+} co-doping due to the overlapping of charge-transfer bands of O^{2-} to Mo^{6+}, O^{2-} to Dy^{3+}, and O^{2-} to Zn^{2+}. The intensity of absorption peak enhances with the co-doping of Zn^{2+} ions up to Z0.25 phosphor and thereafter reduces on further increasing the co-doping concentration. This increased absorbance suggests an enhancement in photoluminescence emission intensity.

The optical bandgap (E_g) of all prepared phosphors was calculated via "Wood and Tauc" method given as[185];

$$(\alpha h\nu)^{1/n} = C\left(h\nu - E_g\right) \quad 6.3$$

Where α and ν are the coefficient of absorbance and frequency of the incident photon, respectively. h is a plank's constant. C is proportionality constant. The exponent value n depends on the nature of the bandgap transition. The $CaMoO_4$ shows an allowed direct transition therefore the exponent n is ½ [18]. In the plot $(\alpha h\nu)^2$ versus $h\nu$, the bandgap of all the phosphors were estimated by extrapolating the linear fitted regions to $(\alpha h\nu)^2 = 0$, as shown in Fig. 6.7(c). The obtained optical bandgap for CMO phosphor is 3.83 eV. A decrease in bandgap up to 3.43 eV is observed with Dy^{3+} doping (as shown for the Dy4 sample in Fig. 6.7(c)). The Zn^{2+} co-doping in Dy4 phosphor leads to a further decrease in bandgap up to 3.26 eV. The decrease in bandgap may be due to an increase in covalent bond length between cations (Mo^{6+}) and anions (O^{2-}) under the influence of dopant and co-dopant ions. With the increase in bond length, the width of the conduction band increases, this reduces the gap between the conduction band and the valence band, as a result, the bandgap decreases [208]. The corresponding bond lengths of Mo—O bonds for CMO, Dy4,

and Z0.25 samples are 1.784 Å, 1.830 Å, and 1.848 Å, respectively, tabulated in Table 6.2. The decrease in the bandgap of the phosphors indicates that oxygen defects are reducing, which can also be verified by the reduction in the intensity of oxygen vacancy peaks in the O1s XPS spectra. This factor helps in enhancing the PL emission intensity of Dy4 phosphor with Zn^{2+} co-doping.

The photostability of the Z0.25 phosphor has been analyzed by recording the absorption at 314 nm over 1 second intervals for 300 minutes. Fig. 6.8 shows that the absorption is very stable; with a linear fit that yields a straight line at 0.4474 for the entire 300 minutes (The slope of the linear fitted line is 5.423×10^{-8} which is nearly zero). Thereby, this confirms the high photostability of the Z0.25 phosphor.

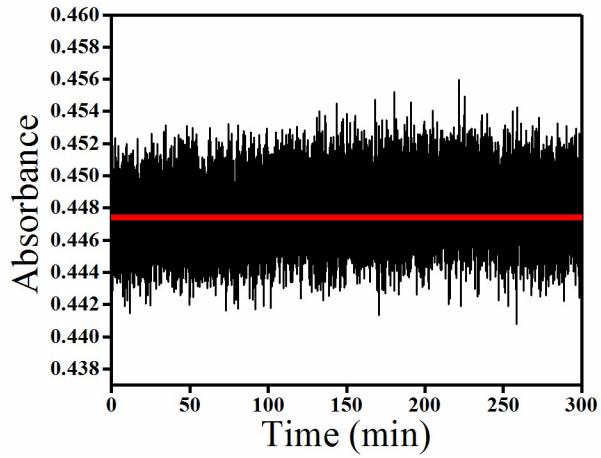

Fig. 6.8 Absorbance at 314 nm with time for Z0.25 phosphor.

6.2.8 Photoluminescence analysis

6.2.8.1 Excitation (PLE) spectra

Fig. 6.9 shows the Photoluminescence excitation (PLE) spectra of CMO, Dy^{3+} doped, and Zn^{2+} co-doped CMO. The obtained PLE spectrum of the CMO sample in Fig. 6.9(a), depicts a broad excitation band centered at 287 nm for CMO recorded for 500 nm emission peak.

This excitation band arises due to the charge transfer from the fulfilled orbital of O^{2-} ions to the partially filled orbital of Mo^{6+} ions[185]. The PLE spectra for Dy^{3+} doped and Zn^{2+} co-doped samples are obtained by examining the $^4F_{9/2} \rightarrow {}^6H_{13/2}$ (574 nm) emission transition of Dy^{3+} ion, depicted in Fig. 6.9(d and e), respectively. The excitation band of the Dy^{3+} doped samples shows an asymmetric nature, which was deconvoluted in two symmetric bands by using the Gaussian fit technique, shown in Fig. 6.9(b). The first symmetric band centered at 287 nm is attributed to the O^{2-} to Mo^{6+} charge transfer band and the second band centered at 300 nm corresponds to the O^{2-} to Dy^{3+} charge transfer band. A redshift is obtained in the emission band of the Dy^{3+} doped samples attributed to the overlapping of both charge transfer bands. Similarly, the excitation band of Zn^{2+} co-doped samples also shows an asymmetric nature which decomposes into three symmetric bands centered at 287 nm, 300 nm, and 318 nm, as depicted in Fig. 6.9(c). These symmetric bands corresponds to $O^{2-} \rightarrow Mo^{6+}$, $O^{2-} \rightarrow Dy^{3+}$, and $O^{2-} \rightarrow Zn^{2+}$ charge-transfer bands, respectively. In Fig. 6.9(d), the intensity of the PLE spectra continues to increase up to 4% doping of Dy^{3+} ions, after which the intensity decreases due to concentration quenching. This indicates that the 4% Dy^{3+} doped (Dy4) sample gives better results in PL emission than the other Dy^{3+} doped samples. Fig. 6.9(e) depicts that the broadband in the Z0.25 sample has the maximum intensity as compared to other Zn^{2+} co-doped phosphors. Some other Dy^{3+} ion transitions are observed in the PLE spectra of Dy^{3+} doped and Zn^{2+} co-doped samples, related to f—f transitions from $^6H_{15/2}$ ground level to $^6P_{3/2}$, $^6P_{7/2}$, $^6P_{5/2}$, $^4I_{13/2}$, $^4G_{11/2}$, $^4I_{15/2}$, and $^4F_{9/2}$ excited levels with corresponding peak position nearly at 327 nm, 357 nm, 371 nm, 392 nm, 430 nm, and 458 nm, respectively. These obtained peaks of Dy^{3+} excitation transitions are well matched with earlier reported papers[18,209].

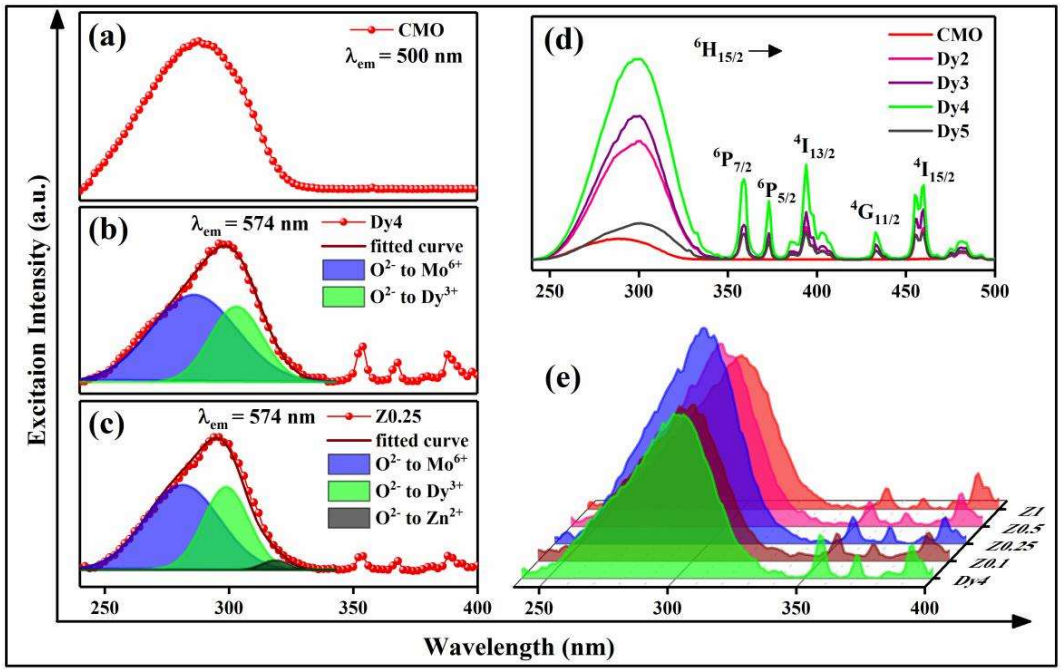

Fig. 6.9 PL excitation spectra for **(a)** CMO, **(b)** Dy4, **(c)** Z0.25, **(d)** (x% = 0, 2, 3, 4, 5) Dy^{3+} doped $CaMoO_4$, and **(e)** (y% = 0, 0.1, 0.25, 0.5, 1) Zn^{2+} co-doped $CaMoO_4$:4%Dy^{3+} phosphors.

6.2.8.2 Emission (PL) spectra

The photoluminescence emission (PL) spectra of CMO, Dy^{3+} doped, and Zn^{2+} co-doped samples have been recorded under the near-UV excitation (287 nm) of the host. In Fig. 6.10(a), the obtained PL spectrum of the CMO phosphor depicts a broadband emission centered at 500 nm, attributed to the energy transfer from the conduction band to the valence band of $[MoO_4]^{2-}$ ions [18,135]. After the Dy^{3+} doping, the intensity of the broad emission band reduces with an increase in doping concentration of Dy^{3+} ions, as depicted in Fig. 6.10(b), which validates the effective energy transfer from $[MoO_4]^{2-}$ to Dy^{3+} energy levels. Moreover, the two prominent bands appearing at 487 nm (blue) and 574 nm (yellow), observed in Dy^{3+} doped phosphors, are ascribed to $^4F_{9/2} \rightarrow {}^6H_{15/2}$ and $^4F_{9/2} \rightarrow {}^6H_{13/2}$ transitions of Dy^{3+} ions, respectively [18,195,196]. The $^4F_{9/2} \rightarrow {}^6H_{15/2}$ (blue) transition is related to a magnetic dipole transition, while $^4F_{9/2} \rightarrow {}^6H_{13/2}$ (yellow) transition is related to

an electric dipole transition. The $^4F_{9/2} \rightarrow {}^6H_{13/2}$ ($\Delta J=2$) transition is a very sensitive electronic dipole transition, allowed at lower symmetry with a non-inversion centre and it is strongly influenced by the chemical environment. Whereas $^4F_{9/2} \rightarrow {}^6H_{15/2}$ transition is a magnetic dipole transition and is less sensitive to the chemical environment. Since the ionic radius of Dy^{3+} ions (1.02 Å, CN=8) is nearly equal to the radius of Ca^{2+} ions (1.12 Å, CN=8), the Dy^{3+} ions are more easily substituted at the lower symmetric positions of Ca^{2+} ions (with a non-inversion center). Hence, the $^4F_{9/2} \rightarrow {}^6H_{13/2}$ electric dipole transition of Dy^{3+} is a more intense emission compared to $^4F_{9/2} \rightarrow {}^6H_{15/2}$ magnetic dipole transition. The emission intensity of the Dy^{3+} transition increases continuously with increasing up to 4% concentration of Dy^{3+} ions. After further increasing the Dy^{3+} concentration, the PL intensity of emission spectra decreases. This phenomenon is known as quenching which may be due to the two reasons; first is the energy exchange from the overlapping of the Dy^{3+} wave functions, and the second is the electrical multipolar transitions of the Dy^{3+} ions. The energy exchange depends on the relative distance between the Dy^{3+} ions and it should be less than 5 Å. The critical relative distance (R_c) between activator ions can be calculated by using the given expression[13,184];

$$R_c = \sqrt[3]{\frac{6V}{\pi x_c N}} \qquad 6.4$$

where x_c represents the critical concentration of Dy^{3+} ions which is 0.04, V is the unit cell volume of x_c% Dy^{3+} doped phosphor (for Dy4 phosphor, $V = 312.2304$ Å^3 as obtained from XRD analysis), and N is the number of host cations per unit cell (for $CaMoO_4$ host $N = 4$). After evaluation, the critical relative distance (R_c) is 15.5 Å (greater than 5 Å), which suggests that non-radiative energy transfer is not attributable to the energy

exchange between Dy^{3+} wave functions. Thus, the quenching phenomenon occurs due to only multipolar electric transitions of Dy^{3+} ions.

The PL emission spectra for Zn^{2+} co-doped phosphors are depicted in Fig. 6.10(d). The PL emission intensity of Dy^{3+} transitions enhances up to 0.25% concentration of Zn^{2+} ions. The corresponding enhancement of intensity is a result of the replacement of Ca^{2+} sites by Zn^{2+} ions. The substituted Zn^{2+} ions absorb energy and transfer it to Dy^{3+} ions which improves the emission transition of Dy^{3+} ions. When increasing the Zn^{2+} concentration, the energy-transfer probability from Zn^{2+} ions to Dy^{3+} ions decreases. Therefore, the non-radiative decay rate increases because the energy transfer among the levels of Zn^{2+} ions increases and the PL emission of Dy^{3+} transitions reduces. The second reason for the improvement in the emission intensity by Zn^{2+} co-doping could be the change in the crystal field around the Dy^{3+} ions causing an increase in asymmetricity. The asymmetry arises because the electric dipole transition of Dy^{3+} ions is affected by the change in crystal field, while the magnetic dipole transition is less affected [109]. For Z0.25, 34% enhancement in the $^4F_{9/2} \rightarrow {}^6H_{13/2}$ peak is observed. The asymmetry around the Dy^{3+} ions is the area ratio of the electric dipole transition and magnetic dipole transition peaks, as given below[45];

$$Asymmetric\ ratio\ (A_r) = \frac{\int_{585}^{560} I_e d\lambda}{\int_{493}^{472} I_m d\lambda} \qquad 6.5$$

where I_e and I_m are the intensity of electric dipole $^4F_{9/2} \rightarrow {}^6H_{13/2}$ transition and magnetic dipole $^4F_{9/2} \rightarrow {}^6H_{15/2}$ transition of Dy^{3+} ions, respectively. The asymmetric ratio (A_r) for Dy4, Z0.1, Z0.25, Z0.5, and Z1 samples are 1.96, 2.46, 3.05, 1.95, and 1.88, respectively. The increased value of A_r suggests a higher degree of covalency between the Dy^{3+} and O^{2-} ions, thereby increasing the interaction strength of the Dy^{3+} ions with the $CaMoO_4$ host

[210].The A_r of Z0.25 is a maximum which leads to stthe ongest interaction between host and Dy^{3+} ions. Hence, the intensity of Dy^{3+} ion emission transition increases.

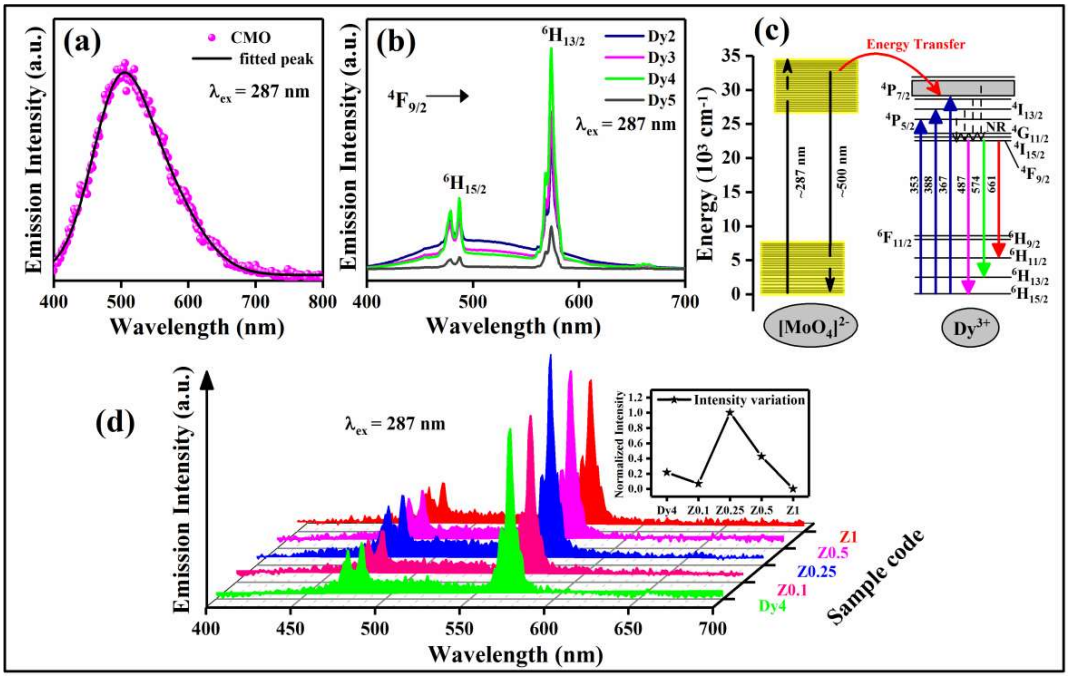

Fig. 6.10 PL emission spectra for **(a)** CMO, **(b)** (x% = 0, 2, 3, 4, 5) Dy^{3+} doped $CaMoO_4$ phosphors, **(c)** Energy level diagram of $[MoO_4]^{2-}$ and Dy^{3+}, **(d)** Emission spectra for (y% = 0, 0.1, 0.25, 0.5, 1) Zn^{2+} co-doped $CaMoO_4$:4%Dy^{3+} phosphors. Inset represents intensity variation of 574 nm peak.

6.2.8.3 PL decay analysis

The normalized PL lifetime decay for Dy4 and Zn^{2+} doped phosphors from $^4F_{9/2}$ to $^6H_{13/2}$ level under 353 nm excitation in logarithmic scale are shown in Fig. 6.11(a). The decay curves are well fitted with the bi-exponential equation given below [184,211];

$$I(t) = I_0 + A_1 exp^{-\left(\frac{t}{\tau_1}\right)} + A_2 exp^{-\left(\frac{t}{\tau_2}\right)} \quad 6.6$$

where $I(t)$ is intensity after time t and I_0 is background intensity after a long time; τ_1, τ_2 are represent fast and slow decay times and A_1, A_2 are their corresponding amplitude.The

value of τ_1, τ_2, A_1, and A_2 are tabulated in Table 5.5. The average decay lifetime is calculated by using the following expression[184,212];

$$\tau_{avg} = \frac{A_1\tau_1^2 + A_2\tau_2^2}{A_1\tau_1 + A_2\tau_2} \quad 6.7$$

Since there are multiple emission quenching centers present in the crystal, a part of energy of the excited ions is transferred to these quenching centers, giving non-radiative emission. Therefore, these defects enhance the non-radiative emission and reduce the lifetime of the emitting ions. The calculated average lifetime from the above expression for Dy4, Z0.1, Z0.25, Z0.5, and Z1 phosphors are 0.655, 0.752, 0.761, 0.756, and 0.722 msec, respectively. The lifetime range is well-matched with previously reported for another Dy^{3+} doped phosphor [212]. The calculated average lifetime of the $^4F_{9/2}$ level of the Dy^{3+} ion increases up to Z0.25 phosphor. The increase in lifetime is due to the enhancement in crystallinity with the Zn^{2+} co-doping. The similar behaviour of improved crystallinity is also verified by the XRD analysis. The enhancement in crystallinity suggests an increase in the particle size, which indicates that the total surface area of the particles per grain boundaries reduces. Thereby reducing the number of defect centers present in the total surface of the particle per grain boundaries, consequently decreasing the number of ions interacting with the defect centers which reduces the non-radiative transitions. Therefore, the lifetime of the $^4F_{9/2}$ level of the Dy^{3+} ions increases for the Z0.25 phosphor. The increase in lifetime suggests that the improvement in crystallinity can also be one of the reasons for improved luminescence in Z0.25 phosphor.

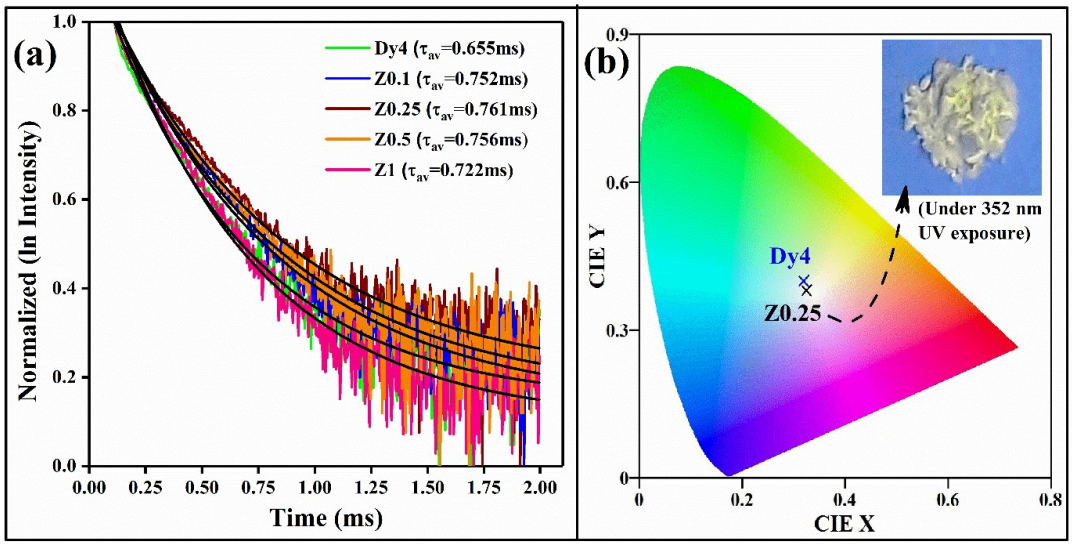

Fig. 6.11(a) PL decay curve and exponential fitted line of Dy4, Z0.1, Z0.25, Z0.5, and Z1 phosphors, **(b)** Chromaticity diagram for Dy4 and Z0.25. Inset shows the image of Z0.25 phosphor under 352 nm UV exposure.

Table 6.5 Fast and slow decay time and their corresponding amplitude.

Sample code	τ_1 (ms)	τ_2 (ms)	A_1	A_2	τ_{av} (ms)
Dy4	0.6549	0.6547	0.4398	0.4820	0.655
Z0.1	0.7519	0.7518	0.3823	0.4046	0.752
Z0.25	0.7611	0.7608	0.3973	0.3997	0.761
Z0.5	0.7559	0.7557	0.4082	0.4325	0.756
Z1	0.7220	0.7218	0.4258	0.4452	0.722

6.2.9 Chromaticity parameters

The chromaticity diagram for Dy4 and Zn0.25 is depicted in Fig. 6.11(b). The Commission Internationale de l'Elcairage (CIE) coordinates of samples in the chromaticity diagram show the actual color of overall emission, correlated color temperature (CCT), and color purity of mono chromaticity, which is summarized in Table 6. The CIE coordinate of the Dy4 phosphor is (0.323, 0.400), which corresponds to a near-white color. The CIE coordinate of the Z0.25 phosphor (0.319, 0.381) is shifted more towards the white illuminant point.

The CCT (in Kelvin) represents color temperature related to emitting light of phosphor, and is evaluated by the following expression [64];

$$CCT = 437n^3 + 3601n^2 + 6861n + 5524.31 \quad 6.8$$

where $n = \frac{x-0.3320}{0.1858-y}$ and the (x,y) are the CIE coordinates of Zn^{2+} co-doped phosphors. The calculated CCT of all Zn^{2+} co-doped phosphors is in the range of 5500 K to 6000 K, which validates that the overall emission is in the white-light field.

The color purity determines the purity of monochromatic emitting light in percentage, evaluated by the following expression [213];

$$color\ purity = \frac{\sqrt{(x_s-x_i)^2+(y_s-y_i)^2}}{\sqrt{(x_d-x_i)^2+(y_d-y_i)^2}} * 100 \quad 6.9$$

where (x_s, y_s) and (x_i, y_i) are the CIE coordinates of the phosphor and the CIE white illumination coordinate (0.3101, 0.3162) in the 1931 CIE Standard chromaticity diagram, respectively. The (x_d, y_d) coordinate is obtained by expanding a straight line from the (x_s, y_s) point to the perimeter through the (x_i, y_i) point. The low color purity percentage represents weak monochromaticity and better white light. The calculated color purity of Dy4 phosphor is 20.3%. After Zn^{2+} co-doping color purity decreases up to 10.7% for the Z0.25 phosphor, which confirms that the overall white emission is improved in the Z0.25 phosphor. The color purity of all Zn^{2+} co-doped phosphors is listed in Table 6.6.

Table 6.6 Chromaticity parameters for Dy4, Z0.1, Z0.25, Z0.5, and Z1 phossphors.

Sample	CIE x	CIE y	CCT (K)	Color Purity (%)
Dy4	0.323	0.400	5500	20.3
Z0.1	0.322	0.392	5865	14.5
Z0.25	0.319	0.381	5994	10.7

Z0.5	0.325	0.387	5765	13.8
Z1	0.325	0.383	5766	12.9

Several Dy^{3+} doped phosphors have been previously reported for white light-emitting applications, whose comparative study of chromatic parameters with Z0.25 phosphor is done in Table 6.7. It is evident that the Z0.25 phosphor has better color purity than the previously reported Dy^{3+} doped phosphors. Therefore, the Z0.25 phosphor is the better candidate for wLEDs.

Table 6.7 Comparison table for chromatic parameters with Z0.25 phosphor.

Phosphor	CIE coordinate (x, y)	Color purity (%)	Ref.
Dy^{3+} doped $Ca_2MgSi_2O_7$	(0.466, 0.429)	68.7	[214]
Dy^{3+} doped $LiSr_4(BO_3)_3$	(0.266, 0.291)	26.3	[190]
Dy^{3+} doped Sr_2SiO_4	(0.282, 0.279)	26	[201]
Dy^{3+} doped $Ba_3Y(PO_4)_3$	(0.347, 0.381)	18.5	[215]
Dy^{3+} doped $CaGd_2ZnO_5$	(0.369, 0.358)	18.2	[216]
Dy^{3+} doped $NaSrB_5O_9$	(0.299, 0.298)	15	[217]
Z0.25	(0.319, 0.381)	10.7	This work

6.2.10 Temperature-dependent PL (TDPL) analysis

The temperature-dependent PL emission in the temperature range of 303–503 K has been analyzed to investigate the thermal stability of the Z0.25 phosphor. Fig. 6.12(a) shows that the integrated PL intensity gradually reduces with increasing temperature due to the thermal quenching phenomena. Fig. 6.12(b) shows the chromaticity diagram where CIE coordinates of the emission intensity for Z0.25 phosphor at different temperatures are plotted. The CIE coordinates at room temperature are (0.32, 0.38), and a negligible changes have been observed in the CIE coordinates with increasing temperature. Therefore, the

rising temperature does not change the overall color emitted by the phosphor, indicating its good thermal stability. The integrated PL intensity at 423 K is 77% of the integrated emission intensity at 303 K, as shown in Fig. 6.12(c). Therefore, there is a 23% loss of emission intensity because of thermal quenching, which is better than commercial $YAG:Ce^{3+}$ and some other reported phosphors [143,163,164,218].

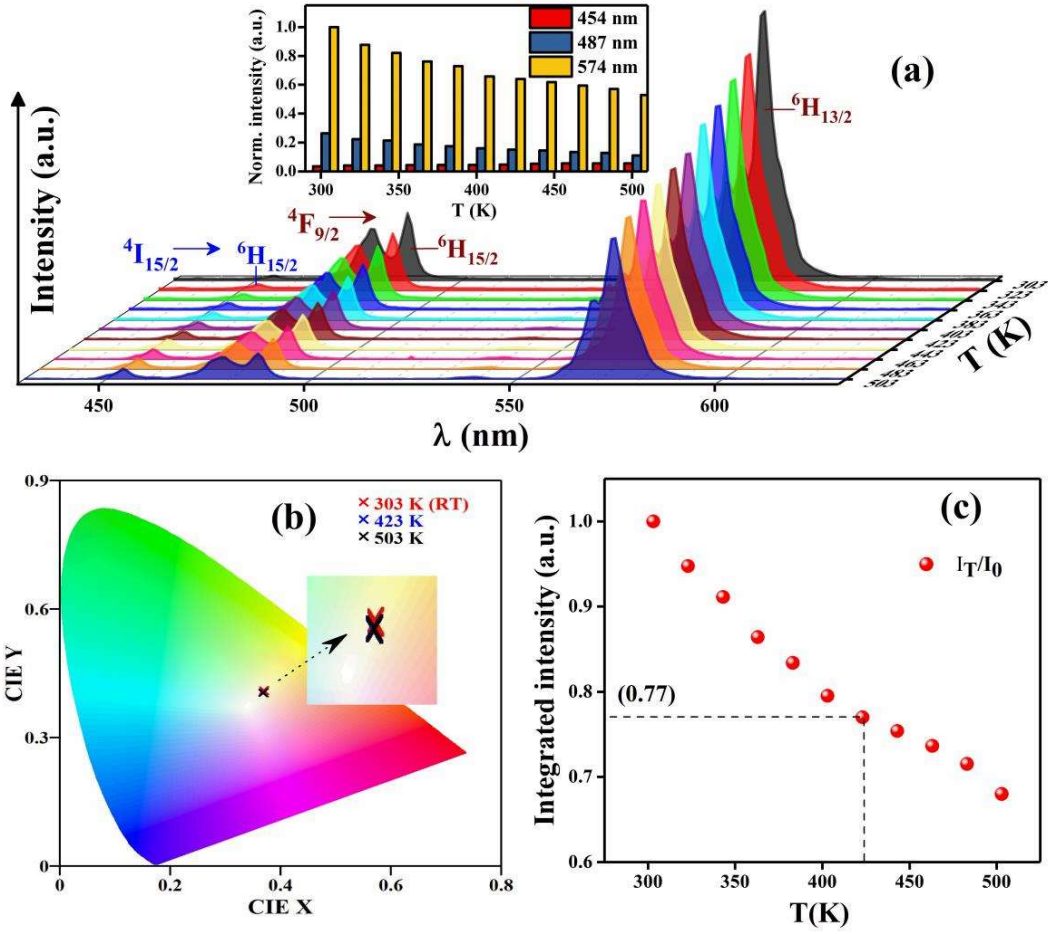

Fig. 6.12 (a) TDPL spectra of Z0.25 phosphor. Inset: Bar diagram depicting intensity variation with temperature, **(b)** Chromaticity diagram depicting variation in CIE coordinates with temperature, and **(c)** Normalized integrated intensity versus T (K) for Z0.25 phosphor.

The PL thermal quenching phenomena can be explained in Fig. 6.13(a). E_L and E_U represent the ground and excited parabolic state, respectively, which intersect at point P. The barrier between the bottom of the excited state (E_U) and point P is the required energy for thermal

quenching, known as thermal activation energy (E_A). The E_L state electrons jump to the E_U state by absorbing the photon's energy (E_I). The energy of the electrons is then partially transferred to spin-lattice vibrations at room temperature, which relaxes them to the equilibrium state by following the non-radiative transition (path 1). After that, the electrons return to the E_L state by the radiative transition (path 2). The strength of the lattice vibration increases with increasing temperature, thereby increasing the active no of phonons. Some of the electrons present at the bottom of the E_U state interact with the active phonons to reach the barrier height P, from where the electrons return to the E_L state by following the non-radiative transition (path 3), leading to thermal quenching. As the temperature rises, the electron-phonon interaction increases, thereby increasing the number of electrons crossing the barrier height (E_A) as a result of which thermal quenching increases.

The E_A required for thermal quenching in the emission spectra can be calculated from the following Arrhenius equation [143],

$$I_T = \left(\frac{I_0}{1 + Ce^{-\left(\frac{E_A}{kT}\right)}} \right) \qquad 6.10$$

where I_0 and I_T are the emission intensity at 303 K and T K, respectively. k and C are the Boltzmann constant and the frequency factor constant, respectively. The $ln\left(\frac{I_0}{I_T} - 1\right)$ versus $\frac{1}{kT}$ the plot is fitted by a linear equation as shown in Fig. 6.13(b), whose slope gives the value of E_A. The calculated value of E_A for the Z0.25 phosphor is 0.16 eV which is higher than previously reported Dy^{3+} doped phosphor[219]. The comparatively high value of thermal activation energy of Z0.25 phosphor exhibits good thermal stability. Thus, the overall emission color stability with temperature makes it a potential phosphor for wLED application.

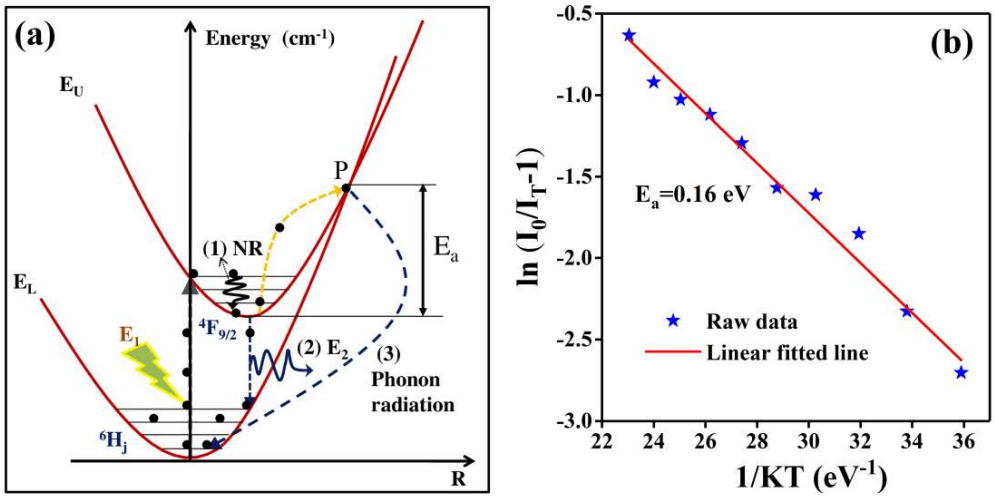

Fig. 6.13 (a) Configurational coordinate diagram, and **(b)** The determination of activation energy for Z0.25 phosphor.

6.3 Conclusions

In summary, all phosphors are successfully prepared by a lucrative auto-combustion process. From structural analysis, it is clear that the dopants have been successfully substituted in the site of Ca^{2+} ions and the structure of $CaMoO_4$ is tetragonal. The SEM and TEM analysis confirm the spherical-shaped morphology of the particles. The XPS scan verifies the chemical state of presented elements in the CMO, Dy4, and Z0.25 samples, and also shows a decrease in oxygen vacancies with Dy^{3+}/Zn^{2+} doping that increase photoluminescence. The major two peaks at 484 nm ($^4F_{9/2} \rightarrow {}^6H_{15/2}$) and 574 nm ($^4F_{9/2} \rightarrow {}^6H_{13/2}$) in the PL emission spectra of Dy^{3+} doped $CaMoO_4$ phosphors are observed under near-UV light radiation (300 nm). The PL emission intensity of the Dy4 phosphor is enhanced after Zn^{2+} co-doping due to a change in asymmetricity around the Dy^{3+} ions. Similarly, the PL lifetime of the $^4F_{9/2}$ level of the Dy^{3+} ion increases after Zn^{2+} co-doping due to the improvement in crystallinity. This shows that the number of defect centers

present in the total surface of the particle is decreasing. As a result, there is a reduction in non-radiative emissions which is responsible for increasing PL emissions. From the chromaticity diagram, it is clear that the overall emission of the Z0.25 phosphor is shifted more toward the white light as compared to the Dy4 phosphor. The temperature-depended PL spectra indicate good thermal stability with high activation energy (0.16 eV) and only a 23% loss of emission intensity at 423 K. The absorbance spectrum at 314 nm for 5 hours indicates the high photostability of Z0.25 phosphor. Thus, with a facile synthesis process, intense white light emission, and good thermal stability, the Z0.25 phosphor is a potential candidate for wLED application.